An analysis of SS precursors using spectral-element method seismograms

L. Bai, Y. Zhang and J. Ritsema

Department of Geological Sciences, University of Michigan, Ann Arbor MI 48109, USA. E-mail: lingb@umich.edu

SUMMARY

The traveltimes of underside shear wave reflections (i.e. SS precursors) are widely used data for mapping the topography of mantle discontinuities in the upper mantle. Here, we examine the accuracy of ray theory in estimating the contribution of shear velocity heterogeneity in the mantle to SS–S400S, SS–S670S and S400S–S670S traveltimes. We analyse stacks of spectral-element method waveforms computed for 34 shallow earthquakes and 16 020 globally distributed virtual seismometers. The waveforms are computed for three versions of shear velocity model S20RTS with variable strengths of the volumetric shear velocity perturbations within the layered structure of the Preliminary Reference Earth Model. We find that ray-theoretical corrections account for only 50 per cent of the traveltime variation due to large-scale velocity heterogeneity. For current tomographic models, as represented by S20RTS, this translates into unpredictable long- and short-wavelength errors in maps of mantle discontinuity depths of about 5 km. This amounts to roughly 10 per cent of published variations in mantle discontinuity depths. However, relative errors will be significantly larger if ray-theoretical traveltime corrections are based on (forthcoming) models of shear velocity with much stronger heterogeneity at the smallest scales.

Key words: Phase transitions; Body waves; Computational seismology; Wave propagation.

1 INTRODUCTION

Waveform stacking of SS precursors is a widely used seismological technique for the imaging of the transition zone (TZ) in the upper mantle. The seismic phase SS is an underside shear wave reflection off Earth's surface halfway between an earthquake and seismic station (Fig. 1). The SS signal on a transverse component seismogram has a relatively high amplitude over a broad teleseismic distance range (70°–160°). SS can be analysed for seismograms for a diverse set of earthquake-station pairs that render a global distribution of SS reflection points.

Underside reflections off the Moho (i.e. SmS) and off seismic discontinuities in the upper mantle (i.e. S400S and S670S) at 400 and 670 km depth—depths according to Preliminary Reference Earth Model (PREM; Dziewonski & Anderson 1981)—are recorded up to 4 min before SS, hence the name 'precursors'. Although these internal reflections have small amplitudes, summation (i.e. stacking) of tens to hundreds of seismograms can bring precursory signal above noise level. The stacking of precursors is, in principle, a straightforward procedure because S670S and S400S have predictable slownesses (i.e. wave incidence angles) and they are not obscured by major high-amplitude phases.

SS precursor analysis yields excellent constraints of the upper mantle beneath both continental and oceanic regions. After the global studies by Shearer (1991) and Shearer & Masters (1992),

the analysis of SS precursors progressed rapidly. A large number of studies have linked seismic reflections to the mineral structure of the upper mantle, the presence of melt and discontinuity topography on a global and regional scale. For reviews, see Shearer (2000), Helffrich (2000), Kind & Li (2007) and Deuss (2009).

SS precursors are particularly useful for estimating the depths of the 400 and 670 boundaries and for estimating the role of the TZ in heat and mass transfer between the upper and lower mantle. The 400- and 670-km discontinuities are usually interpreted as the phase transitions in olivine. The thermodynamic Clapeyron slopes of the 400 and 670 have opposite signs (e.g. Katsura & Ito 1989; Bina & Helffrich 1994; Frost 2008). As a result, the 400 is expected to be shallower and the 670 is expected to be deeper in relatively cool TZ regions (such as subduction zones). Vice versa, in relatively warm mantle regions, the 400 is deeper and the 670 is shallower than the global average values.

The traveltime differences between SS, S400S and S670S are the key probes of mantle discontinuity depths and, indirectly, temperature variations within the TZ. As discussed by Deuss (2009), the TZ is estimated to be, on average, 242 ± 2 km thick, nearly 30 km thinner than in PREM. The 670 is deepest beneath subduction zones (e.g. Flanagan & Shearer 1998; Gu *et al.* 2003; Houser *et al.* 2008; Lawrence & Shearer 2008) and the 400 is deepest beneath the Pacific (e.g. Deuss 2007; Gu *et al.* 2009; Houser & Williams 2010). The long-wavelength variation in TZ thickness of about
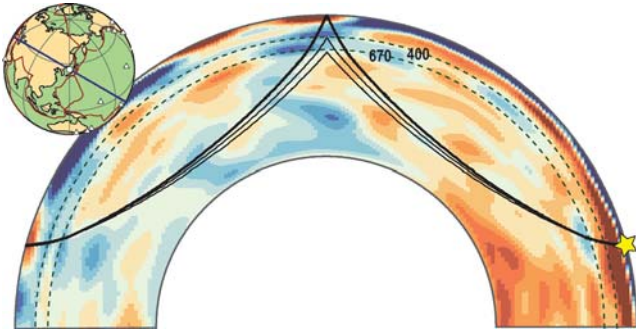
Figure 1. Ray paths of SS, S400S and S670S for an epicentral distance of 160°. The background shows the shear velocity perturbations (low-velocity and high-velocity anomalies in red and blue, respectively) from PREM in a mantle cross-section beneath the western Pacific and eastern Asia (see inserted map) according to model T2. The dashed lines are the 400 and 670 discontinuities.

50 km correlates with the velocity variations seen tomographically and reflect large-scale upper-mantle dynamics. The missing correlation between 400 and 670 topography may be expected if one considers variations of the geotherm across the entire upper mantle (e.g. Ritsema *et al.* 2009b). In addition, mantle discontinuity topography may be complicated by the transformation of garnet (e.g. Hirose 2002) or the effects of mechanical mixing (Xu *et al.* 2008).

Another source of uncertainty arises from the contribution of shear velocity heterogeneity in the crust and mantle on the traveltimes of SS and its precursors. Although numerous studies suggest that ray-theoretical traveltime calculations may be imprecise due to the long-wavelength nature and the broad sensitivity kernels of SS waves (Chaljub & Tarantolla 1997; Neele *et al.* 1997; Neele & de Regt 1999; Zhao & Chevrot 2003; Dahlen 2005), traveltime contributions due to shear velocity heterogeneity has so far been estimated by ray tracing through tomographic velocity models. A notable exception is the study of Lawrence & Shearer (2008) who analyse stacks of waveforms under the assumption that its sensitivity can be approximated by a stack of sensitivity kernels.

Here, we examine the potential errors in depth estimates of the 400 and 670 as inferred from SS precursor analysis when ray theory and long-wavelength tomographic models are used to estimate the contribution of shear velocity heterogeneity to traveltimes. We complement theoretical work (e.g. Zhao & Chevrot 2003; Dahlen 2005) with a study of synthetic seismograms that mimics the analytical procedures commonly applied to data. We compute spectral-element method (SEM) waveforms for three tomographic models and determine how inaccurate ray-theoretical corrections project as artefacts in traveltime maps of synthetic waveform stacks.

2 THREE-DIMENSIONAL WAVE SIMULATIONS AND PROCESSING

We employ the SEM developed by Komatitsch & Tromp (2002) to compute hour-long transverse-component waveforms. With computational resources available to us, we can compute teleseismic seismograms at frequencies shorter than about 60 mHz. This upper limit of the frequency band is sufficiently high to synthesize the relatively long-period waveforms of SS and its precursors. The waveforms are bandpass filtered using a cosine-square filter with cut-off frequencies of 4 and 50 mHz and corner frequencies of 8 and 40 mHz.

We compute waveforms for three 3-D models, which we refer to as T1, T2 and T3 (Fig. 2). T1, T2 and T3 are models of shear velocity

perturbations in the mantle from the transversely isotropic PREM. They are derived from the same data and modelling approaches used to derive model S20RTS (Ritsema *et al.* 2004) but the damping in the tomographic inversion has been adjusted following Ritsema *et al.* (2007). T2 is the same as S20RTS. Models T1 and T3 are more strongly and weakly damped models. Therefore, shear velocity variations in T1 are smoother and weaker than in S20RTS and they are the strongest in model T3. Models T1 and T3 represent the variation in the strength of shear velocity heterogeneity as resolved by the most recently derived global models. We do not modify the seismic structure of the crust nor do we modify the depths of the 400 and 670 velocity discontinuities. Thus, T1, T2 and T3 include only volumetric perturbations of shear velocity that are embedded in PREM's layered structure.

We simulate waveforms for 34 globally distributed earthquakes at a uniform depth of 20 km (Fig. 3). The earthquakes have the same (vertical dip-slip) mechanism as event 101607I (2007 October 16 21:05:43) from the global CMT catalogue to maximize the teleseismic SS radiation. We compute transverse component seismograms at 16 020 virtual seismic stations on a global grid with $2° \times 2°$ spacing. We examine seismograms at source–receiver distance from 110° to 170° and exclude distance ranges where the SS precursors are overlapped with the topside multiples. This yields a fairly uniform distribution of SS reflection points and a density that exceeds 700 per $10° \times 10°$ across the globe.

2.1 Definitions of traveltime anomalies

Differences in traveltimes between SS (T_{SS}), S400S (T_{S400S}) and S670S (T_{S760S}) are defined as

$$\Delta T_{400} = T_{SS} - T_{S400S} \tag{1}$$

and

$$\Delta T_{670} = T_{SS} - T_{S670S}, \tag{2}$$

and the difference traveltime between S400S and S670S is defined as

$$\Delta T_{400-670} = T_{S400S} - T_{S670S}. \tag{3}$$

ΔT_{400} and ΔT_{670} are the two-way traveltimes of shear waves between the surface and the 400 and 670, respectively. $\Delta T_{400-670}$ is the two-way shear wave traveltime through the TZ.

Anomalies of these traveltimes with respect to the PREM are defined as

$$\delta T^{1D} = \Delta T^{SEM} - \Delta T^{PREM}, \tag{4}$$

and with respect to models T1, T2 and T3 as

$$\delta T^{3D} = \Delta T^{SEM} - \Delta T^{3D}. \tag{5}$$

Here, ΔT applies to either ΔT_{400}, ΔT_{670} or $\Delta T_{400-670}$. ΔT^{SEM} is the traveltime difference measured in the SEM waveforms by waveform correlation. ΔT^{PREM} and ΔT^{3D} are the ray-theoretical traveltimes computed for PREM and for the 3-D models (e.g. T1, T2 or T3) for each ray path. δT^{1D} is expected to reflect the 3-D velocity heterogeneity. δT^{3D} is expected to be 0 if ray theory accurately describes long-period SS traveltimes. Thus, non-zero values of δT^{3D} quantify the inaccuracy of ray-theoretical SS traveltime calculations.

Fig. 4 compares T1, T2 and T3 seismograms for a window that includes the SS, S400S and S670S signals based on an event beneath the North Pacific Ocean and a station beneath the western Indian Ocean at an epicentral distance of 124°. The surface reflection
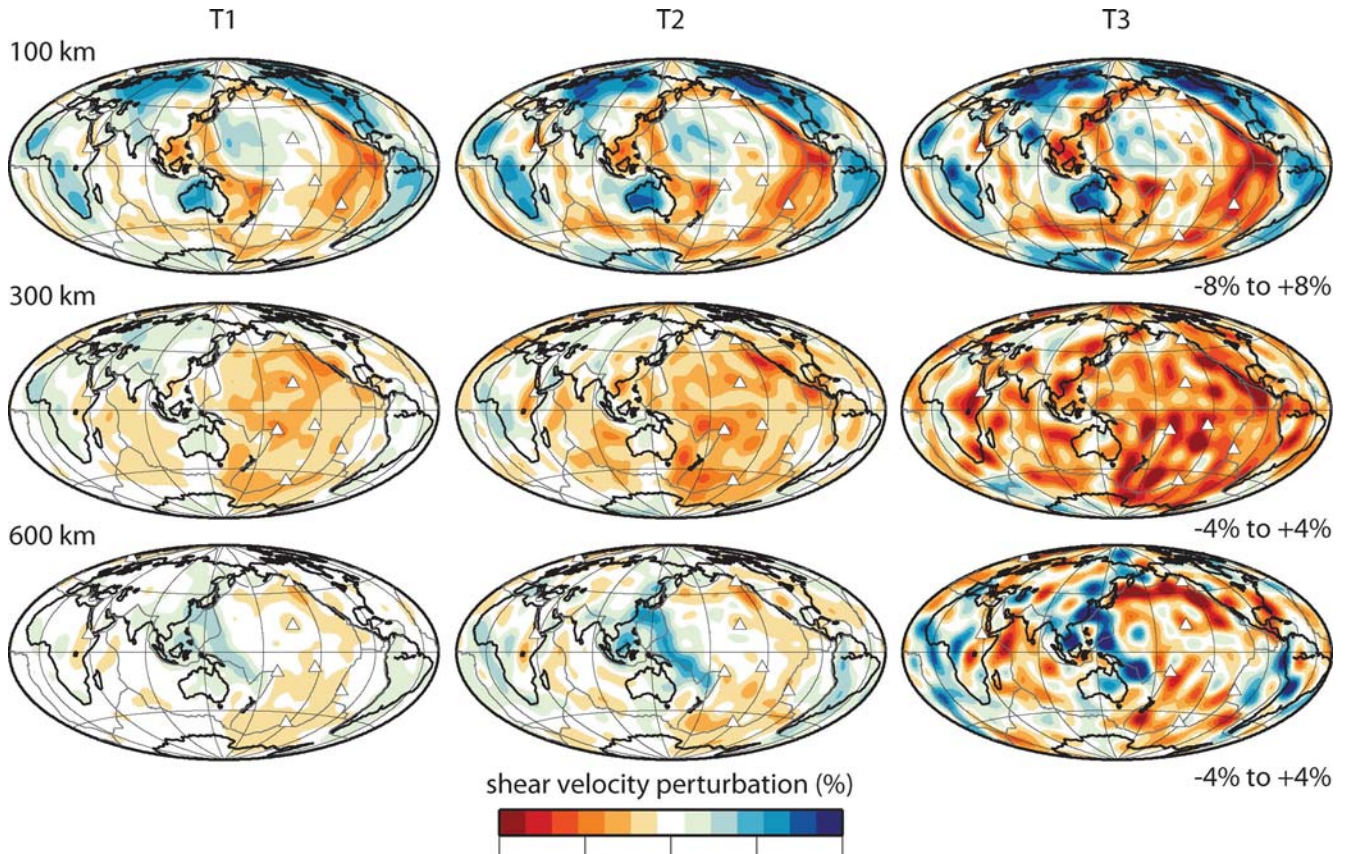
Figure 2. Shear velocity perturbations in the mantle from PREM at (top) 100 km, (middle) 300 km and (bottom) 600 km depth for models (left-hand panels) T1, (middle panels) T2 and (right-hand panels) T3. Low and high shear velocity regions are indicated with red and blue colours. The peak-to-peak variation is indicated below the maps. White triangles are hotspots from the catalogue of Ritsema & Allen (2003).
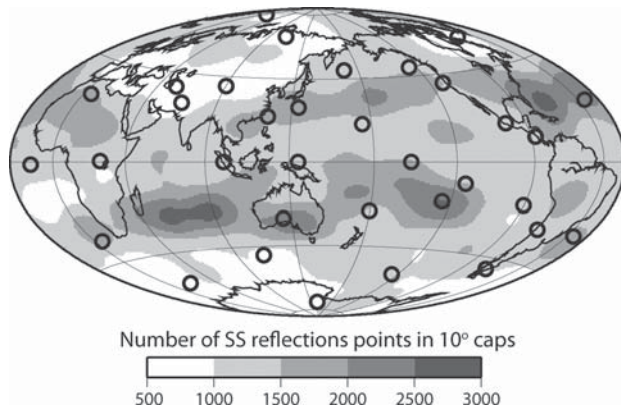
Figure 3. Epicentres of 34 earthquakes (circles) superposed on the global density of the SS bounce points. Note that most regions include more than a 1000 geometric SS surface reflection points within caps with a radius of 10°.

point of SS is at 10°N, 115°E in the South China Sea. Note that $\Delta T_{400-670}$, which can be approximated by the time between the S400S and S670S signal maxima, is several seconds shorter than the PREM and the S20RTS traveltime predictions (i.e. $\delta T^{1D} < 0$ and $\delta T^{3D} < 0$), indicating that ray theory overestimates the shear wave propagation time though the high-velocity TZ beneath the South China Sea. It is this kind of signal that we map using the stacking of SEM waveforms. Note that the S400S and S670S are visible for

all the three models because tomography is smooth and designed to explain global traveltimes.

## 2.2 Stacking and traveltime measurements

The amplitudes of S400S and S670S are only several per cent of the SS amplitude because of the relatively low impedance contrast at the 400 and the 670. When analysing recorded waveforms, trace summation (i.e. 'stacking') is necessary to bring the S400S and S670S signals above noise level. We stack SEM waveforms following a stacking procedure that is commonly applied to data. In this procedure, we align the waveforms on the SS signal, define the arrival time of SS to be 0, multiply waveforms with a negative SS polarity by -1 and normalize the waveforms by dividing them by the peak SS amplitude.

The S400S and S670S waveforms are 120 s long segments centred on PREM-predicted arrival times of S400S and S670S, denoted as τ_{400} and τ_{670} and calculated using the method of Crotwell *et al.* (1999). The stack of the S400S (i.e. S^{400}) and S670S (i.e. S^{670}) signals involves a sum of N traces

$$S^{400}(t) = \sum_{k=1}^{N} s_k\left(t - \tau_{400}^{(k)} - 60, t - \tau_{400}^{(k)} + 60\right), \qquad (6)$$

and

$$S^{670}(t) = \sum_{k=1}^{N} s_k\left(t - \tau_{670}^{(k)} - 60, t - \tau_{670}^{(k)} + 60\right). \qquad (7)$$
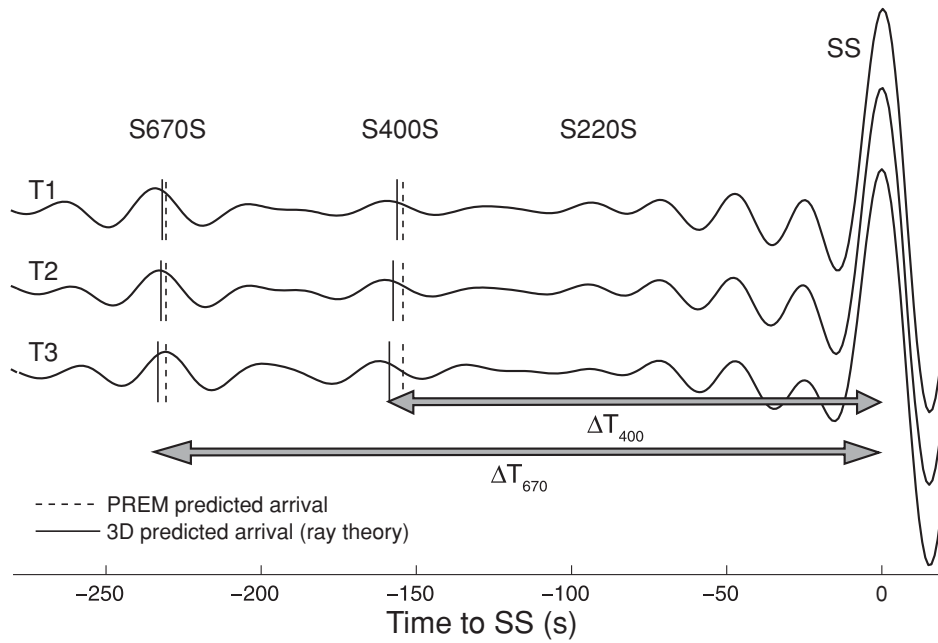
Figure 4. SEM waveforms of SS, S400S and S670S for models T1, T2 and T3, computed for an event beneath the North Pacific Ocean and a station in the western Indian Ocean at an epicentral distance of 124°. The waveforms are aligned on the peak amplitude of SS wave whose arrival time is defined to be 0. The SS surface reflection point is beneath the South China Sea (10°N, 115°E). The S400S and S670S phases arrive about 160 and 230 s before SS. Their PREM and 3-D predicted arrival times are indicated with dotted and solid vertical lines, respectively.

When determining stacks with respect to the ray-theoretical travel-times of models T1, T2 and T3, τ_{400} and τ_{670} are computed by ray tracing through the 3-D models.

The stacks are determined for a selection of N seismograms with common SS reflection points in a circular cap with a midpoint x_0 and a radius of 10°. We map the global variation of δT^{1D} and δT^{3D} by determining stacks for a grid of x_0, uniformly spaced by 5° across the globe. Each of the stacks includes at least $N = 700$ traces (Fig. 3). The traveltimes with respect to PREM (δT^{1D}) and with respect to the 3-D models (δT^{3D}) are estimated by cross-correlating the stacked SS, S400S and S670S waveforms.
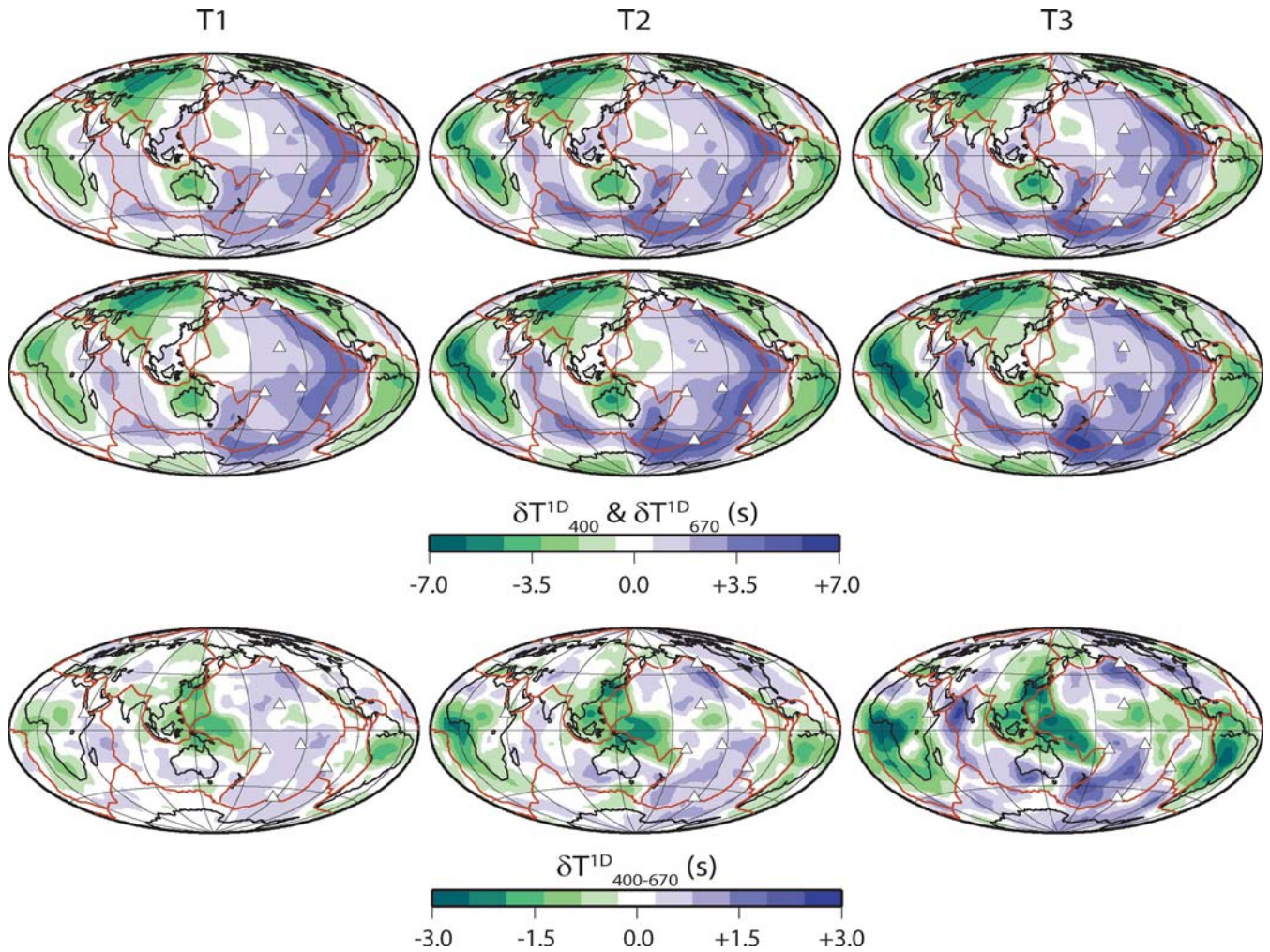
2.3 An analysis of PREM synthetics

To determine artefacts that arise due to the stacking procedure and incomplete data coverage, we first analyse stacks of PREM synthetics. The PREM waveforms have been determined using the transversely isotropic PREM model while the ray-theoretical traveltimes have been calculated for the "equivalent isotropic" PREM model as implemented in the TauP code by Crotwell *et al.* (1999). The slight difference in the implementation of transverse isotropy between 80 and 220 km depths yields a constant traveltime difference of about -1.0 s for δT_{400}^{1D} and δT_{670}^{1D}. This signal has been subtracted from the maps by resetting the mean values of δT_{400}^{1D} and δT_{670}^{1D}.

Fig. 5 shows maps of δT^{1D}, plotted at the cap centres. The variation of δT_{400}^{1D} and δT_{670}^{1D} is less than 0.1 s and the variation in $T_{400-670}^{1D}$ is, at most, 0.2 s. The largest 'traveltime errors' correspond to measurements with relatively low cross-correlation coefficients (<0.9) between the stacked SS, S410S and S660S waveforms and inhomogeneous sampling of the SS slowness range. Nevertheless, the traveltime variation of 0.2 s in these PREM stacks is much smaller than the variation resolved in the stacks of SEM waveforms for T1, T2 and T3. Thus, the signal that we will discuss in the next section does not originate from the stacking method or the inhomogeneous data coverage.
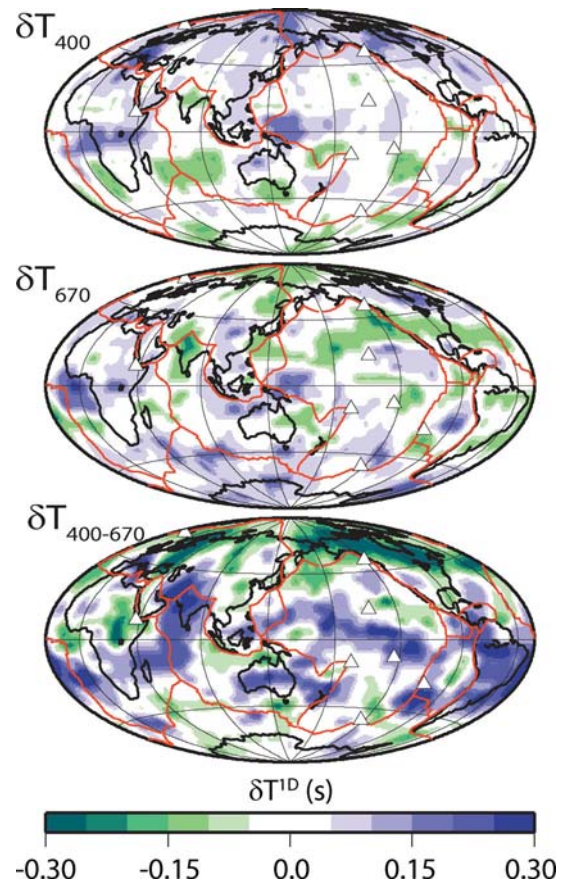
Figure 5. δT^{1D} estimated for PREM synthetics (predicted to be 0) for (from top to bottom) SS–S400S, SS–S670S and S400S–S670S.

T1   T2   T3

δT^{1D}_{400} & δT^{1D}_{670} (s)

-7.0   -3.5   0.0   +3.5   +7.0

$\delta T^{1D}_{400-670}$ (s)

-3.0   -1.5   0.0   +1.5   +3.0

Figure 6. Maps of δT^{1D} for the traveltimes of (from top to bottom) SS–S400S (δT^{1D}_{400}), SS–S670S (δT^{1D}_{670}) and S400S–S670S ($\delta T^{1D}_{400-670}$) for models (left-hand panels) T1, (middle panels) T2 and (right-hand panels) T3. The traveltime variations of δT^{1D}_{400} and δT^{1D}_{670} are two times larger than the variation in $\delta T^{1D}_{400-670}$.

3 RESULTS

3.1 Maps of δT^{1D} and δT^{3D}

Fig. 6 shows maps of δT^{1D} determined from the stacks of the SEM synthetics for models T1, T2 and T3. As expected, the large-scale variation of δT^{1D} is similar to the variations of shear velocity heterogeneity in T1, T2 and T3 (compare Fig. 6 with Fig. 2). Since velocity heterogeneity is largest in model T3, the traveltimes variation is largest for T3. δT^{1D}_{400} and δT^{1D}_{670} are stronger and exhibit longer wavelength variations than $\delta T^{1D}_{400-670}$ because shear velocity heterogeneity in the uppermost mantle is relatively strong and broad.

δT^{1D}_{400} and δT^{1D}_{670} reflect the vertically integrated traveltimes through the upper mantle. The traveltime variation is primarily determined by the strong shear velocity heterogeneity in the uppermost mantle. Hence, the ridges and continents stand out as positive and negative traveltime delays, respectively. $\delta T^{1D}_{400-670}$ correlates with the shear velocity structure in the TZ. It is negative beneath the western Pacific, South America, the central Atlantic and along the Atlantic coasts of Africa. In these regions, the shear velocity is relatively high in T1, T2 and T3.

The amplitude of δT^{3D} ranges from about 1.0 s (for T1) to 3.0 s (for T3) (Fig. 7). This is significantly smaller than the variation of δT^{1D}, which indicates that the ray-theoretical corrections remove a significant portion of the traveltime signal seen in δT^{1D}. It appears that the long-wavelength variations (e.g. subducting zones and ocean–continent contrasts) are explained best by ray theory since a long-wavelength signal in δT^{3D} is not as dominant as in δT^{1D}.

However, the non-zero values of δT^{3D} clearly demonstrate that the ray-theoretical SS traveltimes do not describe the traveltimes of SS and SS precursors exactly. In particular, the peak-to-peak variation in $\delta T^{3D}_{400-670}$ is only a factor of two smaller than the peak-to-peak variation in $\delta T^{1D}_{400-670}$. Moreover, they do not clearly correlate with the shear velocity variations in models T1, T2 and T3 and, therefore, may be interpreted as small-scale thickness variations of the TZ.

3.2 Spectra of δT^{1D} and δT^{3D}

To emphasize that the spatial variation of δT^{3D} comprises a short-wavelength signal in comparison to δT^{1D}, we plot in Fig. 8 the spectral amplitude of $\delta T^{1D}_{400-670}$ and $\delta T^{3D}_{400-670}$ as a function of spherical
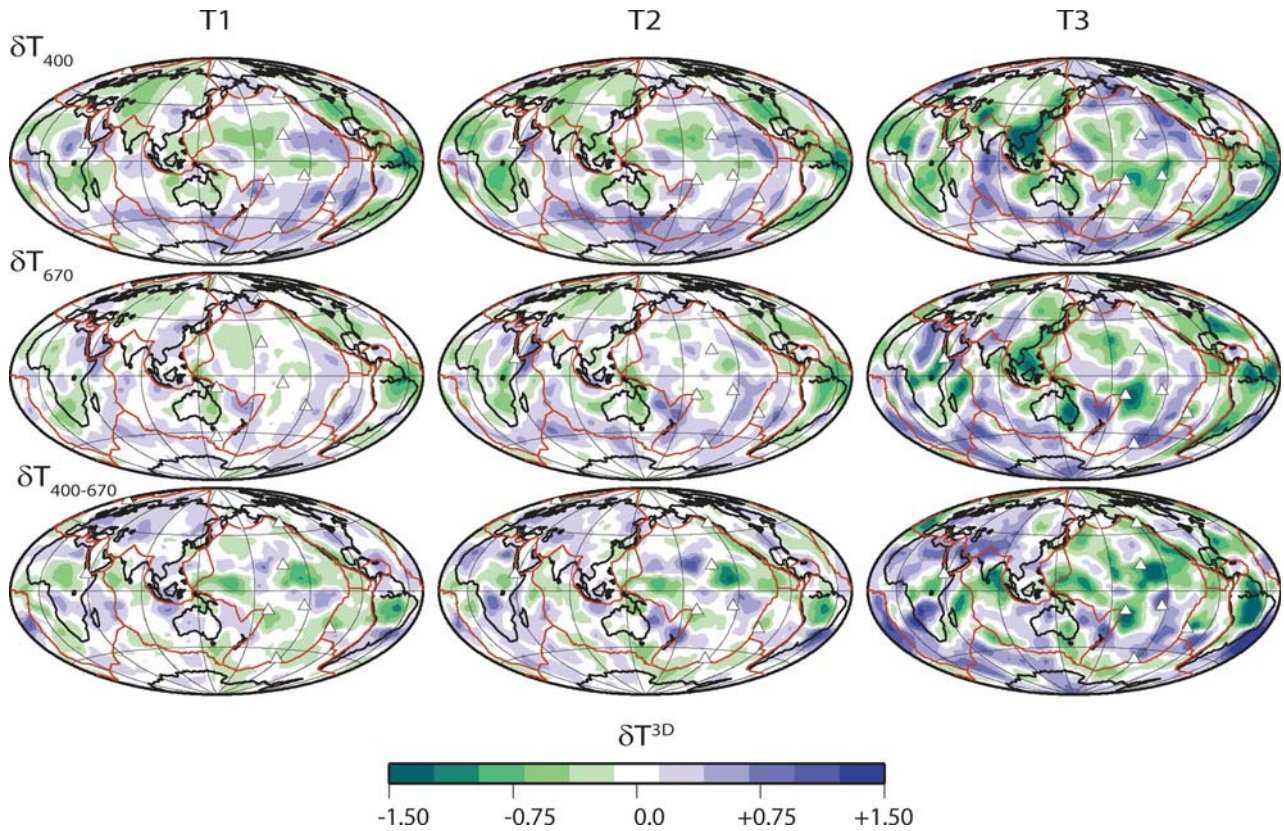
Figure 7. Maps of δT^{3D} for the traveltimes of (from top to bottom) SS–S400S (δT_{400}^{3D}), SS–S670S (δT_{670}^{3D}) and S400S–S670S ($\delta T_{400-670}^{3D}$) for models (left-hand panels) T1, (middle panels) T2 and (right-hand panels) T3.

harmonic degree. These plots are determined by expanding the maps of Figs 6 and 7 into spherical harmonics.

δT^{1D} has a 'red' spectrum that is characteristic for seismic tomography. The S660S–S410S traveltime variations, reflecting the shear velocity variations of the TZ, are the largest for the lowest spherical harmonic degrees. In contrast, the spectrum of δT^{3D} exhibits less variations as a function of spherical order.

From spectra of cap-averaged traveltime maps, it is impossible to determine at which spatial wavelengths the ray-theoretical corrections are incorrect. Nevertheless, Fig. 8 indicates that the 3-D corrected traveltime maps of Fig. 7 includes signals at all spatial wavelengths. The difference in δT^{1D} and δT^{3D} diminishes for increasing spherical order. Beyond about degree 12, the variation of δT^{3D} is as strong as δT^{1D}.

4 DISCUSSION AND CONCLUSIONS

In agreement with Zhao & Chevrot (2003), we find that ray-theoretical traveltime calculations through long-wavelength shear velocity models are imprecise. For three versions of S20RTS in which the strength of shear velocity heterogeneity varies, we find that ray-theoretical calculation of SS traveltimes can differ by several seconds from the traveltimes inferred from SEM seismograms (Fig. 4).

Inaccurate ray-theoretical calculations of traveltimes influence the mapping of the traveltimes of SS precursors (i.e. S400S and S670S) and, hence, the estimates of lateral variations of mantle discontinuity depths.

Our study complements the study from Zhao & Chevrot (2003) by calculating traveltime maps of SS–S400S, SS–S670S and S400–S670S using stacks of SEM seismograms in geographically distributed caps. Traveltimes are 'corrected' for shear velocity heterogeneity by ray tracing through tomographic models. This analytical procedure is similar to the procedures commonly applied to waveform data (e.g. Flanagan & Shearer 1998; Gu & Dziewonski 2002; Houser *et al.* 2008). Fig. 4 indicates that shear velocity heterogeneity, as imaged tomographically, renders minor SS waveform perturbations at frequencies larger than 60 mHz. Therefore, SS and precursor traveltime differences can be determined accurately by cross-correlation analysis.

Since SEM computations are time-consuming, we limit our analysis to three versions of shear velocity model S20RTS, which vary by the amount of damping applied in the tomographic inversion. The variable strength and dominant spatial scales of shear velocity heterogeneity in these three models is similar to the variations within the most recently published tomographic models (e.g. Ritsema *et al.* 2011).

As expected, traveltime anomalies with respect to PREM (Fig. 6), correlate with the shear velocity variations in the uppermost mantle (for δT_{400}^{1D} and δT_{670}^{1D}) and TZ (for $\delta T_{400-670}^{1D}$). The non-zero traveltime variations of δT_{400}^{3D}, δT_{670}^{3D} and $\delta T_{400-670}^{3D}$ demonstrate that ray-theoretical traveltime calculations of SS, S400S and S670S are inaccurate.

The stacking of misaligned S400S and S670S waveforms due to the inaccurate traveltime corrections project as traveltime variations that are 20 per cent (for δT_{400}^{3D} and δT_{670}^{3D}) and 50 per cent (for $\delta T_{400-670}^{3D}$) of the uncorrected signal (i.e. δT^{1D}). Moreover, maps of
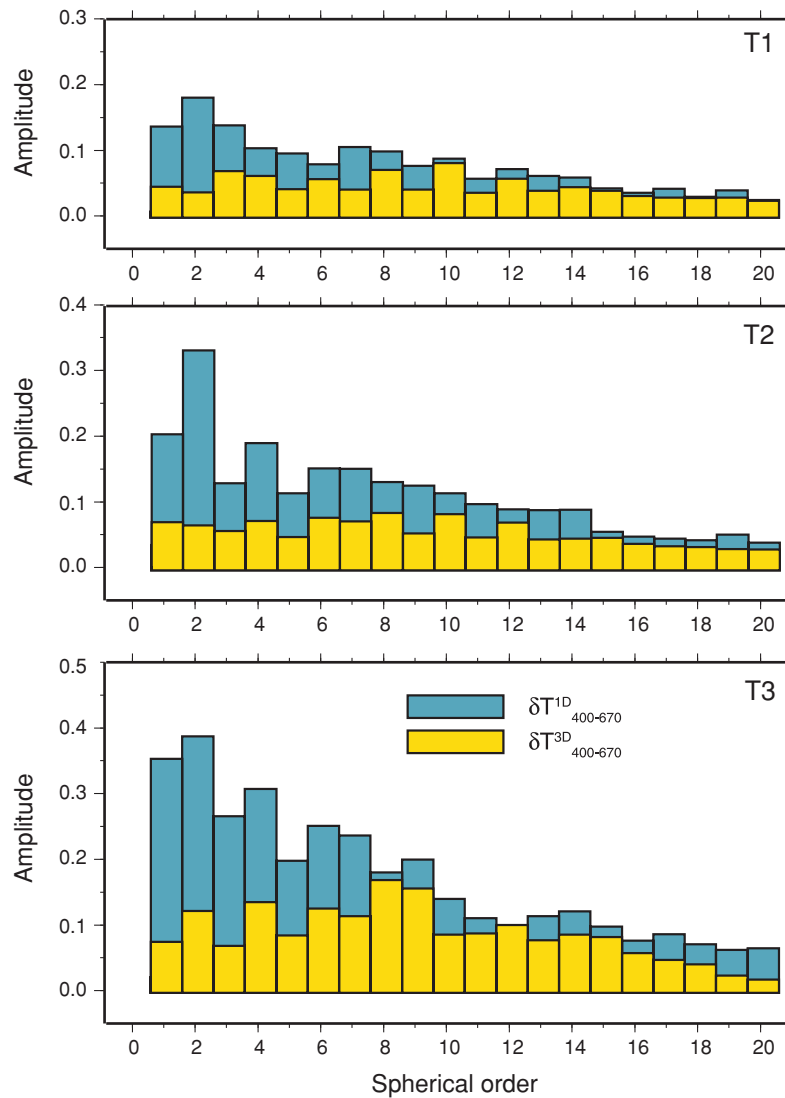
Figure 8. Normalized amplitude spectra as a function of spherical harmonic degree of (blue) $\delta T^{1D}_{400-670}$, and (yellow) $\delta T^{3D}_{400-670}$, for models (top panel) T1, (middle panel) T2 and (bottom panel) T3.

δT^{3D} contain both long-wavelength and short-wavelength structures (Fig. 8). Thus, artefacts in the traveltime maps are not restricted to the short-wavelength structure. Spatial variations in δT^{3D} do not clearly relate to the shear velocity variations in the tomographic model on which they are based and may be misinterpreted as small-scale variations in mantle discontinuity depths.

In waveform data, the variation in $\delta T^{1D}_{400-670}$ is about ± 10 s (e.g. Flanagan & Shearer 1998; Gu & Dziewonski 2002). This is an order of magnitude larger than errors in the ray-theoretical corrections for S20RTS (and other tomographic models) of the upper mantle. Thus, if S20RTS and other recently derived global shear velocity models are adequate models of the shear velocity structure in the upper mantle, inaccuracies in the ray-theoretical corrections do not severely influence the resolution of long-wavelength maps of mantle discontinuity depth. An error in $\delta T^{3D}_{400-670}$ of 1.0 s (Fig. 7) projects as an error in the thickness of the TZ thickness of about 2 km, which is an order of magnitude smaller than the TZ thickness variations inferred from waveform data.

As shown in Fig. 8, the variation in the corrected S400S–S670S traveltime map (i.e. $\delta T^{3D}_{400-670}$) is only smaller than the uncor-rected map (i.e. $\delta T^{1D}_{400-670}$) at the longest wavelengths (<spherical degree 8). Naturally, the use of smaller cap radii or, equivalently, stacking and spatial averaging over smaller regions yields maps of traveltime variations with higher amplitude and more spatial detail. However, as Fig. 9 shows, the errors due to inaccurate traveltime corrections are also amplified. To study small-scale regions of the mantle with SS precursors, such as hotspots (e.g. Deuss 2007), it is necessary to calculate the contribution of the crust (e.g. Ritsema *et al.* 2009a) and shear velocity heterogeneity in the mantle (e.g., Lawrence & Shearer 2008) on traveltimes with finite-frequency approaches.
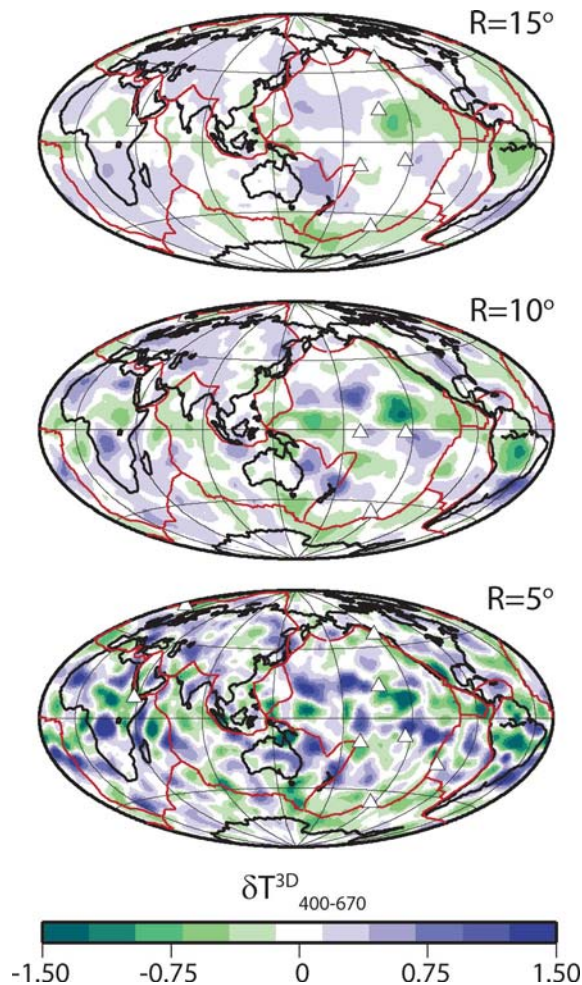
Figure 9. Maps of $\delta T^{3D}_{400-670}$ for model T2 determined by stacking waveforms within caps with radii of (top panel) 15°, (middle panel) 10° and (bottom panel) 5°.

REFERENCES

Bina, C.R. & Helffrich, G., 1994. Phase transition Clapeyron slopes and transition zone seismic discontinuity topography, *J. geophys. Res.*, **99**, 15 853–15 860.

Chaljub, E. & Tarantolla, A., 1997. Sensitivity of *SS* precursors to topography on the upper-mantle 660-km discontinuity, *Geophys. Res. Lett.*, **24**, 2613–2616.

Crotwell, H.P., Owens, T.J. & Ritsema, J., 1999. The Taup toolkit: flexible seismic travel-time and ray-path utilities, *Seismol. Res. Lett.*, **70**, 154–160.

Dahlen, F.A., 2005. Finite-frequency sensitivity kernels for boundary topography perturbations, *Geophys. J. Int.*, **162**, 525–540.

Deuss, A., 2007. Seismic observations of transition zone discontinuities beneath hotspot locations, in *Plates, Plumes, and Planetary Processes*, vol.430, pp. 121–136, eds Foulger, G. & Jurdy, J., GSA, Boulder, CO.

Deuss, A., 2009. Global observations of mantle discontinuities using SS and PP precursors, *Surv. Geophys.*, **30**(4–5), 301–326.

Dziewonski, A.M. & Anderson, D.L., 1981. Preliminary reference Earth model, *Phys. Earth Planet. Inter.*, **25**, 297–356.

Flanagan, M.P. & Shearer, P.M., 1998. Global mapping of topography on transition zone velocity discontinuities by stacking *SS* precursors, *J. geophys. Res.*, **103**, 2673–2692.

Frost, D.J., 2008. The upper mantle and transition zone, *Elements*, **4**(3), 171–176.

Gu, Y.J. & Dziewonski, A.M., 2002. Global variability of transition zone thickness, *J. geophys. Res.*, **107**(B7), 2135, doi:10.1029/2001JB000489.

Gu, Y.J., Dziewonski, A.M. & Ekström, G., 2003. Simultaneous inversion for mantle shear velocity and topography of transition zone discontinuities, *Geophys. J. Int.*, **154**, 559–583.

Gu, Y.J., An, Y., Sacchi, M., Schultz, R. & Ritsema, J., 2009. Mantle reflectivity structure beneath oceanic hotspots, *Geophys. J. Int.*, **178**, 1456–1472.

Helffrich, G., 2000. Topography of the transition zone seismic discontinuities, *Rev. Geophys.*, **63**, 141–158.

Hirose, K., 2002. Phase transitions in pyrolitic mantle around 670-km depth: implications for upwelling of plumes from the lower mantle, *J. geophys. Res.*, **107**(B4), 2078, doi:10.1029/2001JB000597.

Houser, C. & Williams, Q., 2010. Reconciling Pacific 410 and 660 km discontinuity topography, transition zone shear velocity patterns, and mantle phase transitions, *Earth planet. Sci. Lett.*, **296**, 255–266.

Houser, C., Masters, G., Flanagan, M. & Shearer, P.M., 2008. Determination and analysis of long-wavelength transition zone structure using *SS* precursors, *Geophys. J. Int.*, **174**, 178–194.

Katsura, T. & Ito, E., 1989. The system Mg_2SiO_4-Fe_2SiO_4 at high pressures and temperatures: precise determination of stabilities of olivine, modified spinel, and spinel, *J. geophys. Res.*, **94**, 15 663–15 670.

Kind, R. & Li, X., 2007. Deep earth structure—transition zone and mantle discontinuities, in *Treatise on Geophysics*, vol.1, pp. 591–618, eds Schubert, G., Elsevier, B.V., Amsterdam.

Komatitsch, D. & Tromp, J., 2002. Spectral-element simulations of global seismic wave propagation–I. Validation, *Geophys. J. Int.*, **149**, 390–412.

Lawrence, J.F. & Shearer, P.M., 2008. Imaging mantle transition zone thickness with *SdS-SS* finite-frequency sensitivity kernels, *Geophys. J. Int.*, **174**, 143–158.

Neele, F. & de Regt, H., 1999. Imaging upper-mantle discontinuity topography using underside reflection data, *Geophys. J. Int.*, **137**, 91–106.

Neele, F., de Regt, H. & VanDecar, J., 1997. Gross errors in upper-mantle discontinuity topography from underside reflection data, *Geophys. J. Int.*, **129**, 194–204.

Ritsema, J. & Allen, R.M., 2003. The elusive mantle plume, *Earth planet. Sci. Lett.*, **207**, 1–12.

Ritsema, J., Van Heijst, H.J. & Woodhouse, J.H., 2004. Global transition zone tomography, *J. geophys. Res.*, **109**, B02302, doi:10.1029/2003JB002610.

Ritsema, J., McNamara, A.K. & Bull, A., 2007. Tomographic filtering of geodynamic models: implications for model interpretation and large-scale mantle structure, *J. geophys. Res.*, **112**, B01303, doi:10.1029/2006JB004566.

Ritsema, J., Van Heijst, H.J., Woodhouse, J.H. & Deuss, A., 2009a. Long-period body wave traveltimes through the crust: implication for crustal corrections and seismic tomography, *Geophys. J. Int.*, **179**, 1255–1261.

Ritsema, J., Xu, W., Stixrude, L. & Lithgow-Bertelloni, C., 2009b. Estimates of the transition zone temperature in a mechanically mixed upper mantle, *Earth planet. Sci. Lett.*, **277**, 244–252.

Ritsema, J., Deuss, A., Van Heijst, H.J. & Woodhouse, J.H., 2011. S40RTS: a degree-40 shear-velocity model for the mantle from new Rayleigh wave dispersion, teleseismic traveltime and normal-mode splitting function measurements, *Geophys. J. Int.*, **184**, 1223–1236.

Shearer, P.M., 1991. Constraints on upper-mantle discontinuities from observations of long-period reflected and converted phases, *J. geophys. Res.*, **96**, 18 147–18 182.

Shearer, P.M., 2000. Upper mantle seismic discontinuities, *Geophys. Monogr.*, **117**, 115–131.

Shearer, P.M. & Masters, T.G., 1992. Global mapping of topography on the 660-km discontinuity, *Nature*, **355**, 791–796.

Wessel, P. & Smith, W.H.F., 1995. New version of the Generic Mapping Tools released, *EOS, Trans. Am. geophys. Un.*, **76**, 329.

Xu, W., Lithgow-Bertelloni, C., Stixrude, L. & Ritsema, J., 2008. The effects of bulk composition and temperature on mantle seismic structure, *Earth planet. Sci. Lett.*, **230**, 97–112.

Zhao, L. & Chevrot, S., 2003. *SS*-wave sensitivity to upper mantle structure: implications for the mapping of transition zone discontinuity topographies, *Geophys. Res. Lett.*, **30**(11), 1590, doi:10.1029/2003GL017223.